Serine 16 Phosphorylation Induces an Order-to-Disorder Transition in Monomeric Phospholamban†

Emily E. Metcalfe, Nathaniel J. Traaseth, and Gianluigi Veglia*

Department of Chemistry, University of Minnesota, Minneapolis, Minnesota 55455

Received November 18, 2004; Revised Manuscript Received January 5, 2005

ABSTRACT: Phospholamban (PLB) is a 52 amino acid membrane-endogenous regulator of the sarco(endo)-plasmic calcium adenosinetriphosphatase (SERCA) in cardiac muscle. PLB's phosphorylation and dephosphorylation at S16 modulate its regulatory effect on SERCA by an undetermined mechanism. In this paper, we use multidimensional $^{1}H/^{15}N$ solution NMR methods to establish the structural and dynamics basis for PLB's control of SERCA upon S16 phosphorylation. For our studies, we use a monomeric, fully active mutant of PLB, where C36, C41, and C46 have been mutated to A36, F41, and A46, respectively. Our data show that phosphorylation disrupts the "L-shaped" structure of monomeric PLB, causing significant unwinding of both the cytoplasmic helix (domain Ia) and the short loop (residues 17−21) connecting this domain to the transmembrane helix (domains Ib and II). Concomitant with this conformational transition, we also find pronounced changes in both the pico- to nanosecond and the micro- to millisecond time scale dynamics. The $^{1}H/^{15}N$ heteronuclear NOE values for residues 1−25 are significantly lower than those of unphosphorylated PLB, with slightly lower NOE values in the transmembrane domain, reflecting less restricted motion throughout the whole protein. These data are supported by the faster spin−lattice relaxation rates (R_1) present in both the cytoplasmic and loop regions and by the enhanced spin−spin transverse relaxation rates (R_2) observed in the transmembrane domain. These results demonstrate that while S16 phosphorylation induces a localized structural transition, changes in PLB's backbone dynamics are propagated throughout the protein backbone. We propose that the regulatory mechanism of PLB phosphorylation involves an order-to-disorder transition, resulting in a decrease in the PLB inhibition of SERCA.

Phospholamban (PLB)[1] is an integral membrane protein of the cardiac sarcoplasmic reticulum (SR) that is involved in the regulation of intracellular calcium transport. Specifically, PLB inhibits the activity of sarco(endo)plasmic calcium adenosinetriphosphatase (SERCA), thus reducing the rate of calcium uptake into the SR. Upon β-adrenergic stimulation (the "fight or flight" response), PLB is phosphorylated at S16 by cAMP-dependent protein kinase (PKA) and at T17 by Ca/calmodulin-dependent kinase (CAMII). The transfer of a single phosphoryl group at S16 is sufficient to interrupt the inhibition of SERCA by PLB, leading to an increased rate of calcium uptake into the SR and an enhanced rate of cardiac relaxation (*1*).

PLB is an important therapeutic target in the treatment of cardiac disease. Changes in the ratio of PLB to SERCA present in the SR have been observed in mouse models of heart failure (*1*). Gene therapy with a "pseudophosphorylated" PLB mutant, S16E, was found to delay the progression of heart failure in cardiomyopathic hamsters (*2*) and in rats with acquired heart failure (*3*). Moreover, a longitudinal study in two human families revealed that two mutants of PLB, R9C and L39stop, correlate directly with early-onset dilated cardiomyopathy (*4*). Understanding the molecular nature of the interaction between PLB and SERCA as well as PLB's regulatory mechanisms is necessary to pursue these pathways in the treatment of cardiac disease.

Cross-linking and site-directed mutagenesis studies have demonstrated that residues in both the cytoplasmic and transmembrane portions of PLB interact directly with sites on SERCA (*5*, *6*). A recent NMR study mapping the SERCA/PLB binding epitope revealed the existence of residues throughout PLB that are in direct contact with SERCA as well as the involvement of the cytoplasmic domain in the interconversion between different conformations (*7*). While these studies unraveled the molecular details of the contact surface between PLB and SERCA, it is now necessary to understand how phosphorylation changes this interaction. The first step is to define the structure and dynamic behavior of PLB phosphorylated at S16 (pPLB) and to compare these results with those for unphosphorylated PLB.

† This work was supported by grants to G.V. (NIH GM64742). NMR instrumentation was provided with funds from the NSF (BIR-961477) and the University of Minnesota Medical School.

* To whom correspondence should be addressed: Department of Chemistry, University of Minnesota, 207 Pleasant St. SE, Minneapolis, MN 55455. Telephone: (612) 625-0758. Fax: (612) 626-7541. E-mail: veglia@chem.umn.edu.

[1] Abbreviations: CPMG, Carr−Purcell−Meiboom−Gill; MBP, maltose binding protein; NOE, nuclear Overhauser effect; NOESY, nuclear Overhauser effect spectroscopy; TOCSY, total correlation spectroscopy; HSQC, heteronuclear single quantum coherence spectroscopy; NTA, nitriloacetic acid; PLB, phospholamban; TEV, tobacco etch virus; SDS, sodium dodecyl sulfate; DPC, dodecylphosphocholine; SDS−PAGE, sodium dodecyl sulfate−polyacrylamide gel electrophoresis; MALDI-TOF, matrix-assisted laser desorption ionization−time-of-flight; EPR, electron paramagnetic resonance.

10.1021/bi047571e CCC: $30.25
Published on Web 02/22/2005

While wild-type PLB self-assembles into a homopentamer with a small fraction of monomers (*8*), spectroscopic and mutagenesis studies have shown that the monomeric form is the active inhibitory species (*6*, *9*). Mutation of the three cysteines to alanines reverses the tendency to form pentamers, resulting in a predominance of PLB monomers (*10*). This mutation has been shown to retain inhibitory activity against SERCA (*11*). Therefore, our studies have focused on the AFA-PLB mutant, whose three cysteines located in the transmembrane domain (C36, C41, and C46) are mutated to A36, F41, and A46, respectively, which maintains full inhibitory function and is more amenable to spectroscopic studies (*11*, *12*).

The NMR structure of AFA-PLB in dodecylphosphocholine (DPC) micelles was recently solved in our laboratory (*13*). AFA-PLB comprises three structural domains: a transmembrane domain from residues 22 to 52, a connecting loop from 17 to 21, and a cytoplasmic domain from 1 to 17 that is organized into an "L-shaped" structure in which the transmembrane and cytoplasmic domains form an approximately 80° angle (*13*, *14*). Further, our recent $^{1}H/^{15}N$ backbone spin relaxation studies revealed the presence of four dynamics domains in PLB: domain Ia (residues 1−16), a short loop (residues 17−21), and a transmembrane helix split into a flexible domain Ib (residues 23−30), and a motionally restricted domain II (residues 31−52). Moreover, dynamics on the micro- to millisecond time scale were observed throughout the cytoplasmic domain, loop, and flexible portion of the transmembrane domain, revealing an overall plasticity of the protein that might explain its ability to adapt to several different binding partners, including SERCA, protein kinases, and protein phosphatase 1 (*15*).

Here, we report the NMR structure and ^{15}N backbone dynamics of AFA-PLB phosphorylated at S16 (pAFA-PLB). Since phosphorylation at S16 alone has been found to be sufficient to relieve the inhibition of SERCA (*1*), we have chosen to begin our studies by phosphorylating PLB only at S16.

MATERIALS AND METHODS

Expression and Purification of ^{15}N-pAFA-PLB. ^{15}N-Labeled AFA-PLB was expressed and purified as previously described (*16*). TEV protease was expressed and purified as previously described (*17*).

A second purification step was necessary prior to phosphorylation to remove residual detergent from ^{15}N-AFA-PLB. The protein was purified by reversed-phase HPLC on a diphenyl, 5 μm, 4.6 × 250 mm column (Vydac) with a linear gradient over 35 min (solvent A, 95% H_2O, 3% 2-propanol (^{i}PrOH), 2% acetonitrile (ACN), and 0.1% trifluoroacetic acid (TFA); solvent B, 57% ^{i}PrOH, 38% ACN, 5% H_2O, and 0.1% TFA). The protein eluted at 30−31 min and the solvent was evaporated under N_2 gas and then lyophilized. All the solvents were purchased from Fisher Scientific and used without further purification.

Phosphorylation of ^{15}N-AFA-PLB at S16. HPLC-purified ^{15}N-labeled AFA-PLB was reconstituted in 20 mM 3-(*N*-morpholino)propanesulfonic acid (MOPS) at pH 7.3 containing 1% octyl glucoside. To determine the final sample concentration, a Tris−Tricine SDS−12% polyacrylamide gel was used and the protein was quantified by use of a Molecular Imager *FX* (Bio-Rad). The sample was then diluted up to 0.25 mg/mL with MOPS buffer prior to the addition of ATP (1 mM), $MgCl_2$ (1 mM), and 1000 IU of protein kinase A catalytic subunit (Sigma)/mg of AFA-PLB. The mixture was shaken at 30 °C for several hours and purified by fast protein liquid chomatography (FPLC), followed by dialysis and lyophilization. Phosphorylation was confirmed by Western immunoblot with the specific antibodies 1D11 and 285 for PLB and pAFA-PLB, respectively (*18*). The mass of the product was determined by MALDI-TOF mass spectrometry with an α-cyano-4-hydroxycinnamic acid (CCA) matrix. The observed mass of 6296 Da corresponded to the calculated mass of 6293 Da within the expected error.

NMR Spectroscopy. Samples for NMR spectroscopy were prepared by dissolving ^{15}N-labeled pAFA-PLB in 300 μL of phosphate-buffered saline, pH 6.0, containing 300 mM deuterated DPC (Cambridge Isotope Labs) and 5% D_2O. Most of the experiments were performed on a Varian INOVA spectrometer equipped with an inverse-detection triple-resonance probe, operating at 599.90 MHz for ^{1}H and 60.79 MHz for ^{15}N. The exceptions were the ^{15}N-edited NOESY-HSQC and the conformational exchange broadening experiments, which were carried out on a Varian INOVA spectrometer operating at of 800.24 MHz for ^{1}H and 81.10 MHz for ^{15}N. The temperature was held constant at 37 °C. The backbone and side-chain resonance assignments were obtained with an ^{15}N-edited TOCSY−HSQC with a mixing time of 70 ms. NOEs were obtained with ^{15}N-edited NOESY-HSQC experiments with mixing times of 150 and 200 ms. All 3D experiments were recorded with 1024 complex points in the direct dimension, 80 points in the indirect ^{1}H dimension, and 40 points in the indirect ^{15}N dimension. Spectral widths of 8000 Hz in the ^{1}H dimension and 1700 Hz in the ^{15}N dimension were employed. Quadrature detection was accomplished by the States−time-proportional phase incrementation (TPPI) scheme (*19*). ^{15}N decoupling during acquisition was achieved by use of a GARP-1 pulse sequence (*20*). A sensitivity enhancement scheme was used for both 2D and 3D experiments (*21*). All spectra were referenced to the DSS signal (*22*, *23*). All spectra were processed with NMRPipe software (*24*) with a 90°-shifted sine bell function in both dimensions, zero-filled to double the size, and baseline-corrected by use of a polynomial function. The final sizes of the 3D matrixes were 1024 × 160 × 80 real points after zero-filling in both dimensions and the Fourier transformation. Chemical shift assignments, NOE assignments, and peak intensity measurements were accomplished by use of NMRView (*25*).

Structure Calculations. Structure calculations were performed with XPLOR-NIH software (*26*). The initial template for the simulated annealing was an extended conformation of the PLB backbone. An initial high-temperature stage consisting of 2000 restrained molecular dynamics steps of 0.5 fs each was performed at a temperature of 4000 K with all force constants fixed. The cooling stage consisted of 5000 molecular dynamics steps with a 0.5 fs time step. The temperature was decreased from 1000 to 100 K during this interval. A second stage of refinement was carried out with the script refine_gentle.inp to include the full van der Waals potential. Starting from a temperature of 2000 K, the conformers were cooled to 100 K. During the high-temperature steps, the dihedral angles were constrained by

use of a harmonic potential with a force constant of 200 kcal/mol. A final minimization of 500 steps was undertaken with conjugated gradients. A total of 423 NOEs were used in the calculations, of which 173 were intraresidue and 250 interresidue NOEs. Hydrogen-bond constraints were added in the final stage of refinement for both the transmembrane segment and the cytoplasmic helix from residue 4 through 14, and from residue 24 through 49, respectively.

All NOEs were unambiguously assigned. When stereospecific assignments could not be made, pseudoatom corrections were employed via the center of mass approach. Conformers were accepted on the basis of the lowest NOE violations by use of the "accept.inp" routine included in the XPLOR software package. The 40 selected structures showed no NOE violations greater than 0.5 Å, no bond angle violations greater than 5°, and no bond length violations greater than 0.05 Å. The covalent geometry of the conformers generated was analyzed with PROCHECK_NMR (*27*).

Measurement of ^{15}N Backbone Dynamics and Model-Free Analysis. ^{1}H−^{15}N spin relaxation measurements were carried out using two-dimensional, proton-detected heteronuclear NMR experiments, implementing standard pulse sequences based on Farrow et al. (*28*). Spectral widths of 1700 and 7000 Hz were used in the ω1 (^{15}N) and ω2 (^{1}H) dimensions, respectively. ^{15}N decoupling during acquisition was achieved by use of a GARP-1 pulse sequence (*20*). The effects of cross-relaxation between ^{1}H−^{15}N dipolar and ^{15}N chemical shift anisotropy (CSA) were removed by applying ^{1}H 180° pulses during relaxation delays (*29*). ^{1}H−^{15}N steady-state NOE enhancements were measured with no initial proton saturation and then with initial proton saturation to allow NOE evolution. The initial proton saturation period was 3 s. Data were collected with 1024 complex points and employed 256 scans in the ω2 (^{1}H) dimension and 96 points in the ω1 (^{15}N) dimension. R_1 spin−lattice relaxation rates were measured in a series of spectra with relaxation delays of 10 (×2), 20, 40, 180, 300, 500, 800, 1000, and 1100 ms. R_2 spin−spin transverse relaxation rates were measured with relaxation delays of 10 (×2), 30, 50, 70, 90, 110, and 150 ms. For both R_1 and R_2 measurements, the spectra were recorded by 64 scans with 1024 and 64 complex points in the ω2 (^{1}H) and ω1(^{15}N) dimensions, respectively. The relaxation delay for both R_1 and R_2 measurements was 1.5 s.

R_1 and R_2 were fit to a single-exponential decay by use of the Rate Analysis tool in NMRView (*25*). Errors in R_1 and R_2 were estimated by obtaining duplicate spectra with relaxation delays of 10 ms (*30*). The errors in R_1 and R_2 were obtained from the standard deviations of the Monte Carlo simulations (*31*). The error in the ^{1}H−^{15}N steady-state NOE enhancement was estimated from the standard deviation of the baseplane noise in the spectrum without initial proton saturation (*28*).

The relaxation measurements were analyzed with the Modelfree software package (*31*). In this calculation, the entire data set is fit to a model in which the molecule undergoes nanosecond rotational diffusion with a rotational correlation time τ_m, and each residue undergoes its own local motion characterized by one or more order parameters and correlation times that are much shorter than τ_m. Model selection was performed according to Mandel et al. (*32*). A sum-squared error (SSE) was minimized for each residue in each of five possible parameter sets: (1) S^2, (2) S^2 and τ_e, (3) S^2 and R_{ex}, (4) S^2, τ_e, and R_{ex}, and (5) S2s, S2f, and τ_e. S^2 is the generalized order parameter, τ_e is the effective internal correlation time and is on the picosecond time scale, R_{ex} is a chemical exchange term, and S2s and S2f are terms that result from resolving the generalized order parameter into two order parameters. S2s reflects slower motions, and S2f, faster motions. A nonlinear least-squares fit was used to optimize a local correlation time, τ_{loc}, at each residue. In this model, the local correlation time, τ_{loc}, replaces the global correlation time, τ_m, and no global rotational diffusion model is assumed. In each case, 500 Monte Carlo simulations were performed.

Conformational exchange broadening was analyzed by a semiquantitative approach (*33*) to characterize the dynamics of pAFA-PLB on the micro- to millisecond time scale. First, R_2 spin relaxation rates were measured with a composite refocusing pulse during the R_2 evolution period, with a WALTZ-16 proton decoupling scheme to eliminate the effects of ^{1}H−^{15}N scalar coupling, ^{15}N chemical shift anisotropy, and ^{1}H−^{15}N dipole cross-correlation. The R_2 spin relaxation measurements were repeated with a CPMG pulse train during R_2 time (R_2^{CPMG}) to suppress the contributions to the relaxation arising from chemical or conformational exchange. Spectra were acquired with 64 points in the ω1 (^{15}N) dimension and 2048 complex points in the ω2 (^{1}H) dimension, with spectral widths of 1700 and 9000 Hz, respectively. The repetition rate within the CPMG pulse train (τ_p) was measured, and 0.8 ms was determined to be the best value. The relaxation delays for both R_2 and R_2^{CPMG} experiments were 9.6 (×2), 30.4, 49.6, 70.4, 89.6, 110.4, and 150.4 ms.

R_2 and R_2^{CPMG} were fit to single-exponential decay by use of the Rate Analysis tool in NMRView (*25*). Errors were estimated from the standard deviation of the difference in peak heights in duplicate spectra, as described above for R_1 and R_2 (*30*, *31*). The results of these experiments are reported as ΔR_2, the difference between R_2 and R_2^{CPMG}, which is an estimate of the rate of chemical or conformational exchange, R_{ex}.

H/D Exchange Factors. Exchange factors for ^{15}N uniformly labeled pPLB-AFA were determined as described previously (*34*). NMR samples were lyophilized and resuspended in solutions containing 5%, 15%, 30%, and 50% D_2O, respectively, and four ^{1}H/^{15}N HSQC spectra were collected for each D_2O concentration after a fixed 30-min incubation period at 37 °C. The amide intensities for all the spectra were normalized to those measured in the sample with 5% D_2O. The peak intensities were plotted as a function of the mole fraction of H_2O (X) according to

$$(yC)^{-1} = \chi(1 - X)/X + 1$$

where y is the peak volume, C is a normalization factor, and the slope χ is the exchange factor. The errors on the exchange factors were determined from regression analysis on the above equation.

Localization of PLB Cytoplasmic Domain in DPC Micelles. As with the unphosphorylated AFA-PLB, the localization of pAFA-PLB with respect to the micelle surface was established by use of Mn^{2+} as a paramagnetic relaxation agent. The line broadening of the amide resonances in the

HSQC spectra was used to assess the exposure of the amides to the bulk solvent or their position with respect to the hydrocarbon region of the micelles (*35*).

RESULTS AND DISCUSSION

In our structural and dynamics studies, we utilized a biologically active, monomeric mutant of PLB suitable for NMR study, which has three transmembrane cysteine residues mutated to alanine, phenylalanine, and alanine, respectively (AFA-PLB) (*11*, *12*). The original NMR structure and ^{15}N backbone dynamics of this mutant were reported under the following experimental conditions: 600 mM DPC, pH 4.2, 20 mM phosphate buffer, and 50 °C (*13*, *15*). A later study involving direct interactions with the SERCA used conditions of 300 mM DPC, 20 mM phosphate buffer, pH 6.0 at 37 °C found to be favorable for the activity of both proteins (*7*). To verify that no changes in the structure and dynamics were occurring, we repeated both structural and dynamics NMR measurements under these new conditions. The Hα chemical shifts and the NOESY patterns were found to be identical to those under both experimental conditions (data not shown). In this paper, we used the new experimental conditions described above to ensure SERCA activity and PLB inhibitory effects (*7*).

Though the phosphorylation of PLB has been widely studied in cardiac SR homogenates and in vivo cell expression systems, the NMR study of recombinant PLB phosphorylated in vitro has been hindered by the inability to obtain full in vitro phosphorylation of PLB. Under our experimental conditions, we obtained full in vitro phosphorylation of AFA-PLB, as indicated by a gel shift on a Western blot with the PLB-specific antibody 1D11 (*18*) (Figure 1A). The presence of the phosphate group was confirmed by use of the pPLB specific antibody 285 (*18*) (Figure 1B) and by MALDI-TOF mass spectrometry, which verified that the product had the expected mass (Figure 1C).

NMR Solution Structure of pAFA-PLB. The fully S16-phosphorylated AFA-PLB displays a well-resolved NMR spectrum, as shown by the HSQC spectrum in Figure 2. Chemical shift and NOE assignments were accomplished by use of both ^{15}N-edited TOCSY-HSQC and ^{15}N-edited NOESY-HSQC experiments (*21*). ^{15}N-edited NOESY-HSQC experiments were conducted with mixing times of 150 and 200 ms, with similar results. A total of 423 intra- and interresidue NOEs were defined and classified as strong, medium, and weak by use of NMRView software (*25*). Both the backbone NOE pattern and the Hα chemical shift index (CSI) indicate the presence of two helical domains, from residue 4 through 14 and from residue 23 through 50 (Figure 4).

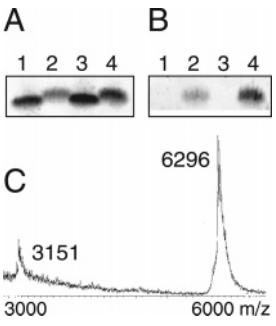

FIGURE 1: Western blot and MALDI-TOF mass spectrometry results characterizing the phosphorylation of AFA-PLB at S16. (A) The characteristic gel shift upon phosphorylation is observed by use of PLB-specific antibody 1D11. (B) The presence of phosphorylation is confirmed by use of the S16 phosphorylated PLB specific antibody 285 (*18*). The samples run on both blots are identical and are labeled: (1) 100 ng of AFA-PLB (control), (2) 100 ng of pAFA-PLB, (3) 200 ng of AFA-PLB (control), and (4) 200 ng of pAFA-PLB. Control samples were prepared exactly as the phosphorylated samples, except that ATP was omitted from the reaction vessels. (C) MALDI-TOF mass spectrometry results of the phosphorylated product, pAFA-PLB. Expected mass: 6293.

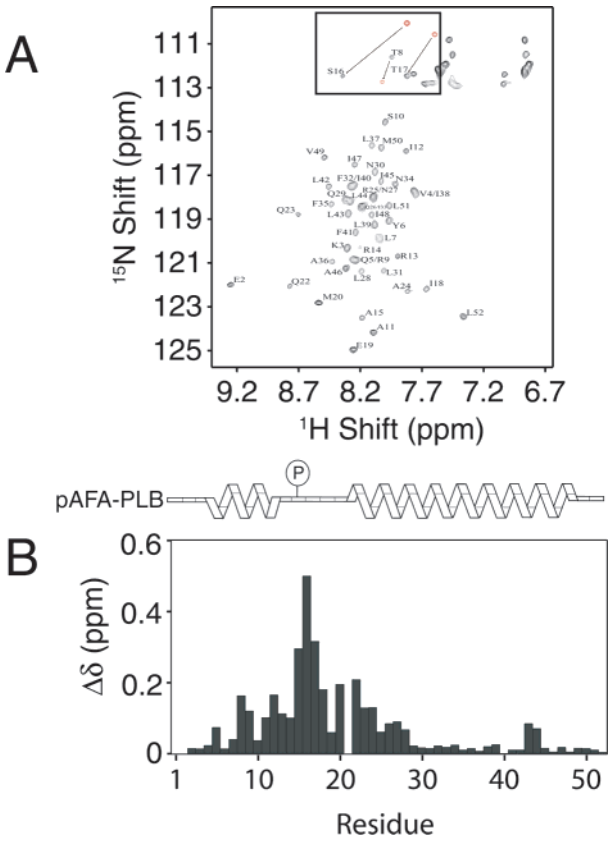

FIGURE 2: (A) Fully assigned ^{1}H−^{15}N HSQC spectrum of pAFA-PLB in 300 mM DPC micelles obtained at 800.24 MHz at 37 °C. For clarity, only the resonances of S16 and T17 from the unphosphorylated form of PLB are superimposed and indicated in the box. (B) Histogram showing the normalized changes in amide chemical shifts upon phosphorylation calculated according to the expression $\Delta\delta = \sqrt{(\Delta\delta_N^2/25+\Delta\delta_H^2)}/2$, where $\Delta\delta_N$ and $\Delta\delta_H$ are the changes in chemical shifts for the nitrogen and proton, respectively.

A comparison of the Hα proton chemical shifts of AFA-PLB and pAFA-PLB immediately reveals a change in secondary structure around the phosphorylation site (Figure 4). AFA-PLB shows strong upfield shifts in the chemical shift index from the N-terminus through residue 17, an indication that this region is α-helical. In contrast, pAFA-PLB shows weak upfield shifts up to residue 12, which gradually evolves in downfield shifts up to residue 22. The Hα chemical shifts of the transmembrane helices for both AFA-PLB and pAFA-PLB are quite similar, showing that this structural element is preserved in both forms. The observation of both $d_{\alpha N}(i, i+1)$ and $d_{NN}(i, i+1)$ NOEs in conjunction with $d_{\alpha N}(i, i+3)$ and $d_{\alpha N}(i, i+4)$ connectivities is diagnostic of a regular α-helix (*36*). We detected several $d_{NN}(i, i+1)$, $d_{\alpha N}(i, i+1)$, and an overlapping series of

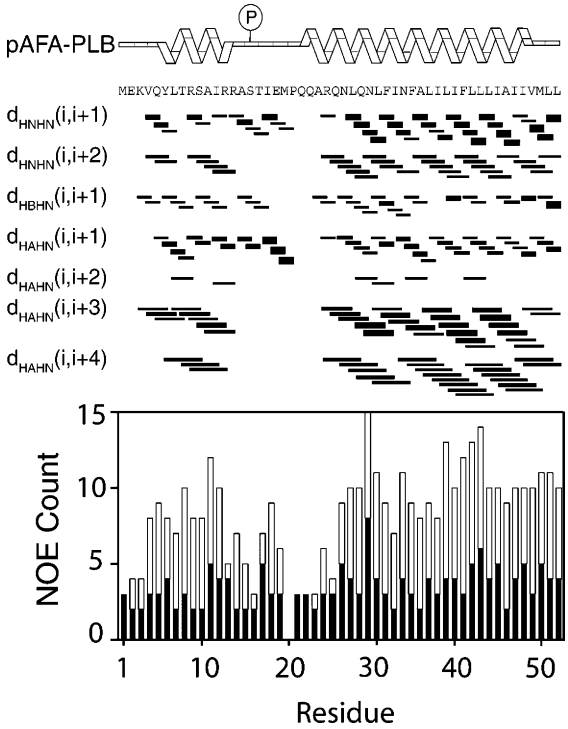

FIGURE 3: (Top) Sequential and medium-range proton−proton backbone NOE connectivities obtained from ^{15}N-edited NOESY−HSQC experiments for pAFA-PLB. Thick, medium, and thin bars represent strong, medium, and weak connectivities, respectively. (Bottom) NOE count versus residue number: intraresidue NOEs are denoted with solid bars, while interresidue NOEs are denoted by open bars.

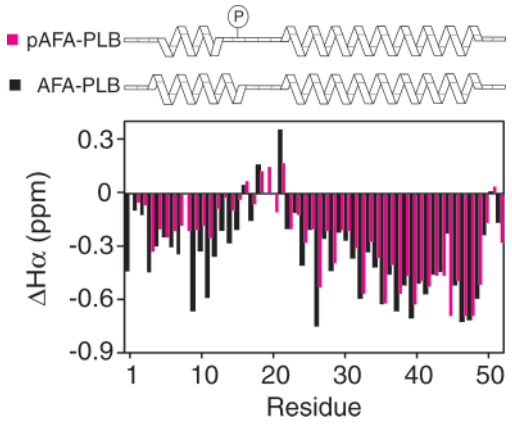

FIGURE 4: Histograms representing Hα chemical shift indices for the phosphorylated and unphosphorylated forms of PLB.

$d_{NN}(i, i + 2)$ involving residues 4−21 and 24−52, while $d_{\alpha N}(i, i + 3)$ and $d_{\alpha N}(i, i + 4)$ connectivities mostly involve residues 4−14 and 24−52. A summary of medium- and short-range NOE connectivities is presented in Figure 3. Most of the NOEs are localized in the two structured regions of PLB, while the relatively long segment encompassing residues 13−23 does not show a substantial number of NOEs. In particular, several $d_{\alpha N}(i, i + 3)$ and $d_{\alpha N}(i, i + 4)$ that were detected for the unphosphorylated form (*13*) are now absent (see Figure 3).

A total of 419 NOEs were used in the structure calculations. The lowest conformational energy structures resulting from our simulated annealing calculations were selected and analyzed. All the structural statistics are reported in Table 1, while Figure 5 shows the superposition of the generated

Table 1: NMR-Derived Restraints and Structural Statistics for the 20 Lowest Energy Conformers

NOE, Hydrogen Bonds and Dihedrals	
total NOE	419
intraresidue	150
interresidue	242
hydrogen bonds	29
dihedral angles (Φ/Ψ)	0
Average Energies (kcal mol^{-1})	
E_{tot}	197 ± 15
E_{NOE}	48 ± 7
E_{bond}	20 ± 1
E_{angle}	111 ± 6
$E_{improper}$	18 ± 1
E_{VDW}	10 ± 4
Restraint Violations	
>0.5 Å	0
RMSD (Å) for Backbone Superposition	
helix 1, residues 3−13	0.50 ± 0.27
helix 2, residues 22−50	0.96 ± 0.40
helix 2, residues 25−50	0.86 ± 0.22
RMSD (Å) for Heavy Atom Superposition	
helix 1, residues 3−13	1.86 ± 0.97
helix 2, residues 22−50	2.06 ± 0.74
helix 2, residues 25−50	1.87 ± 0.35
Ramachandran Analysis (%)	
residues in most favored regions	81.6
residues in additional allowed regions	15.0
residues in generously allowed regions	2.0
residues in disallowed regions[a]	1.5

[a] Residues in disallowed regions are located in the unstructured loop.

structures. As with the unphosphorylated PLB, the backbones of the conformers of the phosphorylated species do not converge to form a tight ensemble of structures. While the superposition of the backbones of the unphosphorylated form gives poor convergence with a RMSD of ∼3.4 Å (*13*), the superposition of the backbones for the phosphorylated species gives ∼6.2 Å RMSD, indicating no convergence (Figure 5A). Only the superposition of the specific domains gives good convergence of both the backbone and side chains (see Table 1). The superposition of the backbones gives a RMSD of 0.50 and 0.86 Å for residues 3−13 and 25−50, respectively. If the structural fitting is performed including residues 22−24 (i.e., from residue 22 to 50), the RMSD increases significantly and becomes 0.96 Å. For the structures of the unphosphorylated AFA-PLB, the superposition of this region gives a RMSD of 0.19 Å, while superposition of residues 22−50 gives a RMSD of 0.48 Å. This shows that the transfer of a single phosphoryl group induces a less defined structure throughout the entire transmembrane domain, and in particular around region 22−24. Interestingly, residues 22−24 of the protein have been shown to be more solvent-exposed and more dynamic than the rest of the transmembrane domain as probed by NMR, EPR, and fluorescence spectroscopy (*15*, *37*, *38*).

These results show that the longer loop induced by phosphoryl transfer results in the loss of structural correlation between the different domains, thereby constituting a point of flexibility between two very well-defined structural domains, a mechanism supported by the spin relaxation measurements (see following sections). The distinct "L-shaped" structure identified in the unphosphorylated form is no longer present upon phosphorylation.

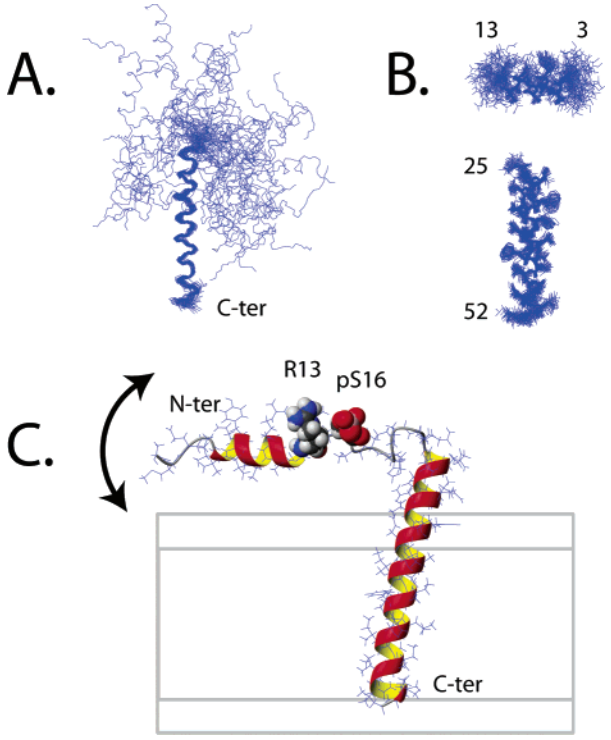

FIGURE 5: (A) Overlay of the backbones for the ensemble of 40 lowest energy conformers generated by the simulated annealing procedure. (B) Top: superposition of heavy atoms (residues 3−13) for the cytoplasmic helix. Bottom: superposition of heavy atoms (residues 22−50) for the transmembrane helix. (C) Cartoon representation of the average minimized structure, evidencing R13 and S16 facing each other.

^{15}N Backbone Dynamics of AFA-PLB Phosphorylated at S16. The relaxation rates, R_1 and R_2, and the heteronuclear steady-state NOE enhancement values for the backbone amides of pAFA-PLB are reported in Figure 6. These values could not be obtained for overlapped residues Q5 and R9, Q26 and I33, and F32 and I40 or for P21 (see Figure 6). The heteronuclear NOE values show rigid motions (NOE ∼ 0.8) in the transmembrane domain (residues 30−52). The cytoplasmic helix has slightly less restricted motions, with NOE values between 0.6 and 0.7. Between residues 12 and 24, NOE values drop to 0.5 or less, reflecting the relatively free motions of this unstructured region. R_1 values average 2−3 s^{-1} up to residue 25. Beyond residue 25 and throughout the transmembrane helix they are consistently around 1 s^{-1}. On the other hand, R_2 values up to residue 18 are very similar to those for unphosphorylated PLB, averaging approximately 15 s^{-1}. Residues 18−20 in the hinge region display much shorter R_2 values (∼10 s^{-1}), while from residue 22−28 the R_2 values return to ∼15 s^{-1}. For the most hydrophobic residues of the transmembrane domain, the R_2 values increase to an average of 20 s^{-1}. Throughout the protein, heteronuclear NOE values are lower for pAFA-PLB than AFA-PLB, with the most significant differences occurring within residues 1−29. Additionally, the NOE value for residue 38 of pAFA-PLB is measurably lower than for the unphosphorylated PLB. A similar NOE value is seen for residue 39 of pAFA-PLB, which is further evidence that pAFA-PLB has more mobility within the first few residues of the transmembrane helix. Taken together, these three data sets (NOE, R_1, and R_2) indicate that phosphoryl transfer to S16 not only causes local

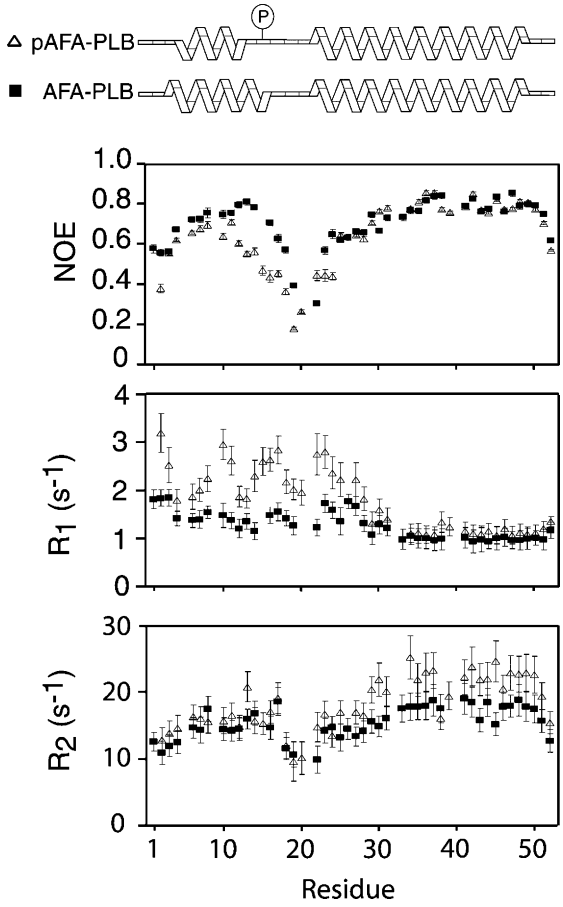

FIGURE 6: ^{15}N backbone dynamics measurements of AFA-PLB and pAFA-PLB in 300 mM DPC micelles obtained at 600 MHz at 37 °C. ^{1}H−^{15}N NOE, R_1, and R_2 values obtained at 600 MHz are plotted by residue number.

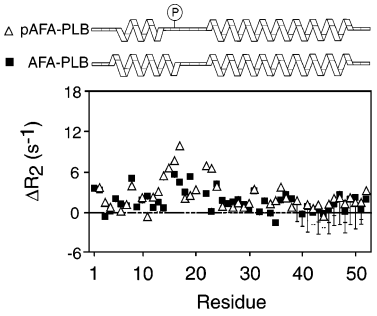

FIGURE 7: Analysis of slow time scale motion for both AFA-PLB and pAFA-PLB: Plot of the difference between ^{15}N R_2^{CPMG} and R_2, performed with and without CPMG pulse train, respectively. Large values of ΔR_2 correspond to conformational exchange broadening caused by motion in the micro- to millisecond time scale.

conformational changes but also causes dynamic changes throughout the entire protein backbone.

Conformational exchange on the micro- to millisecond time scale was measured by the method described by Zuiderweg and co-workers (*33*), which is based on the differences between R_2 (relaxation rates) values, measured by use of a pulse sequence with a single, composite refocusing pulse during the R_2 evolution period, and R_2^{CPMG} values, measured with a CPMG train of pulses substituting for the single pulse. The differences between these R_2^{CPMG} and R_2 values, reported as ΔR_2 in Figure 7, are directly correlated with the R_{ex} terms. Values close to 0 correspond

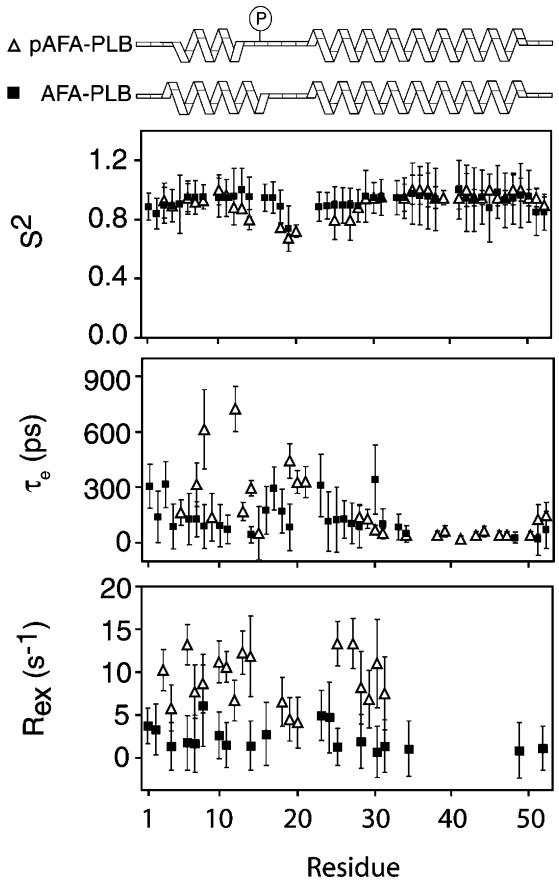

FIGURE 8: Model-free analysis of ^{15}N relaxation data for both AFA-PLB and pAFA-PLB. S^2 (order parameter), τ_e (internal correlation time), and R_{ex} (chemical exchange rate) are plotted according to residue number.

to an absence of dynamics in the micro- to millisecond time scale, while higher values of ΔR_2 indicate conformational exchange. The ΔR_2 values are close to 0 in the two helical regions of the protein. A substantial increase in ΔR_2 is observed around the phosphorylation site spanning residues 14−17. In addition, residues 22−24 also show increased ΔR_2 values. This region has significant dynamics in the unphosphorylated PLB, which is accentuated by the presence of the phosphoryl group. Overall, from the analysis of these data it can be inferred that PLB phosphorylation causes an increase in the micro- to millisecond time-scale dynamics involving the overall motion of domains Ia, Ib, and the loop.

The R_1, R_2, and heteronuclear NOE values were interpreted according to the model-free analysis of Lipari and Szabo (*39*) by use of Modelfree software (*31*) available from Dr. Arthur Palmer at Columbia University. Model selection was achieved according to Mandel et al. (*32*). In accordance with the recently reported model-free analysis of AFA-PLB (*15*), we chose the local diffusion model, which does not assume a single rotational correlation time for the entire protein but rather fits a local correlation time for each residue. Similar fits assuming isotropic or axially symmetric rotational diffusion produced inadequate agreement with the experimental data (high χ^2 values, results not shown). The best data fit was accomplishing by use of a combination of modelfree parameter sets: (1) S^2, (2) S^2 and τ_e, (3) S^2 and R_{ex}, and (4) S^2, τ_e, and R_{ex}. These results are plotted by residue number in Figure 8 and summarized in Tables 2 and 3 for both AFA-PLB and pAFA-PLB. Most residues in the cytoplasmic helix, loop, and the first several residues of the transmembrane helix were fit with model 4, S^2, τ_e, and R_{ex}. The remainder of the transmembrane helix (residues 34−52) was fit with models 1 and 2. Several residues could not be fit with any model. These included E2, R15, S16, T17, N22, N23, and A24. It should be noted that these residues are in unstructured regions, have ^{1}H−^{15}N NOE values lower than 0.5 (Figure 6), and undergo motions on the micro- to millisecond time scale (Figure 7). The relative motional freedom of these residues makes them impossible to fit with any dynamics model.

Table 2: Summary of Modelfree Analysis of pAFA-PLB[a]

residue	model	S^2	dS^2	τ_e (ps)	dτ_e	R_{ex} (s^{-1})	dR_{ex}
K3	3	0.93	0.12			10.1	2.4
V4	4	0.89	0.02	165	69	5.7	3.0
Y6	4	0.95	0.10	316	119	0.0	2.0
L7	4	0.92	0.02	615	216	7.6	3.7
T8	4	0.93	0.01	138	129	8.6	3.0
S10	3	1.00	0.10			11.1	2.5
A11	4	0.96	0.01	726	122	10.5	2.4
I12	4	0.88	0.01	170	48	6.6	2.7
R13	4	0.87	0.01	295	43	12.2	3.0
R14	4	0.80	0.07	52	145	11.8	4.9
I18	4	0.74	0.03	444	95	6.4	3.0
E19	4	0.67	0.03	329	62	4.3	3.6
M20	4	0.72	0.04	331	85	4.0	2.7
R25	3	0.79	0.01			13.3	2.5
N27	3	0.79	0.01			13.3	2.5
L28	4	0.88	0.02	137	64	8.1	3.9
Q29	4	0.94	0.03	130	52	6.7	4.4
N30	4	0.95	0.02	69	25	10.9	4.5
L31	4	0.95	0.02	53	26	7.4	4.2
N34	2	0.95	0.09	42	21		
F35	1	1.00	0.10				
A36	1	1.00	0.10				
L37	1	1.00	0.12				
I38	2	0.95	0.07	42	23		
L39	2	0.95	0.05	63	29		
F41	2	0.95	0.08	21	17		
L42	1	1.00	0.11				
L43	2	0.95	0.06	42	19		
L44	2	0.95	0.05	62	27		
I45	2	1.00	0.12				
A46	2	0.94	0.05	42	21		
I47	2	0.95	0.05	42	20		
I48	1	1.00	0.10				
V49	1	1.00	0.08				
M50	2	0.95	0.06	42	20		
L51	2	0.95	0.06	126	80		
L52	2	0.90	0.06	147	73		

[a] Overlapped residues and residues that could not be fit with any model are excluded from the table.

The S^2 values across the protein show a pattern of restricted motions in the helical regions ($S^2 \sim 0.9$) and increased mobility in the loop region ($S^2 < 0.8$) (Figure 8). The long τ_e values for residues 1−29 indicate less restricted motion than for residues 30−52, which have very short τ_e values (~40 ps). R_{ex} values are the fastest (~12 s^{-1}) in the loop region. The notable exceptions in this region are residues 18−20, which have R_{ex} values between 4 and 6 s^{-1}. This correlates well with the observed ΔR_2 values for these residues, which were significantly lower than for the other residues of the loop region. The absence of the R_{ex} term in the membrane-associated part of the transmembrane helix corresponds well with the low ΔR_2 values observed for this region in the conformational exchange experiments, since the ability to fit these residues with models 1 and 2 is

Table 3: Summary of Modelfree Analysis of AFA-PLB[a]

residue	model	S^2	dS^2	τ_e (ps)	dτ_e	R_{ex} (s^{-1})	dR_{ex}
M1	4	0.89	0.09	306	118	3.6	2.1
E2	4	0.84	0.01	139	139	3.2	3.0
K3	2	0.90	0.12	316	125		
V4	4	0.89	0.11	88	122	1.2	2.8
Q5	1	0.90	0.20				
Y6	4	0.95	0.11	128	139	1.6	3.2
L7	4	0.95	0.12	127	95	1.5	3.4
T8	4	0.95	0.08	88	120	6.0	4.8
S10	4	0.95	0.13	91	115	2.5	2.7
A11	4	0.95	0.13	72	78	1.4	2.6
I12	1	0.96	0.19				
R13	1	1.0	0.14				
R14	4	0.95	0.13	43	44	1.3	2.9
S16	4	0.95	0.09	177	129	2.6	3.7
T17	2	0.95	0.10	295	117		
I18	2	0.89	0.11	171	119		
E19	2	0.74	0.15	84	127		
Q23	4	0.89	0.10	311	169	4.8	3.0
A24	4	0.89	0.09	116	161	4.6	4.1
R25	4	0.90	0.13	125	177	1.1	2.2
Q26	2	0.90	0.12	126	102		
N27	2	0.90	0.11	105	111		
L28	4	0.89	0.11	90	118	1.7	3.2
Q29	1	0.96	0.18				
N30	4	0.95	0.11	342	188	0.5	3.1
L31	4	0.95	0.12	102	82	1.2	3.1
I33	2	0.95	0.12	84	71		
N34	4	0.94	0.14	48	44	0.9	3.3
F35	1	0.98	0.21				
A36	1	0.96	0.20				
L37	1	0.96	0.22				
I38	1	0.94	0.21				
F41	1	1.00	0.20				
L42	1	0.94	0.22				
L43	1	0.94	0.22				
L44	1	0.95	0.18				
I45	1	0.88	0.23				
A46	1	0.98	0.18				
I47	1	0.93	0.18				
I48	4	0.94	0.17	27	31	0.7	3.3
V49	1	0.96	0.22				
M50	1	0.96	0.18				
L51	4	0.85	0.16	21	90	0.9	2.6
L52	2	0.85	0.12	69	100		

[a] Overlapped residues and residues that could not be fit with any model are excluded from the table.

characteristic of the absence of slow dynamics (micro- to milliseconds). Both τ_e and R_{ex} values indicate the presence of additional dynamics on both the pico- to nanosecond and micro- to millisecond time scales for the cytoplasmic helix, which is further supported by the R_1 spin relaxation values. Finally, as shown for the unphosphorylated form of PLB (*15*), there are quantitative discrepancies between the R_{ex} values calculated from the Modelfree approach and the ones determined experimentally. This is due to the approximation we used in the Modelfree approach, which does not take into account the rotational anisotropy of PLB (*15*).

Both H/D exchange factor measurements and paramagnetic mapping experiments support the results obtained for the structure and dynamics of pAFA-PLB. Exchange factors plotted as a function of the residue number show that the hydrogen-bond network around the phosphorylation site has been disrupted by the presence of the phosphoryl group (see Figure 9). In addition, in pAFA-PLB we found higher values of exchange factors in the whole cytoplasmic domains and in domain Ib. This further supports our previous findings

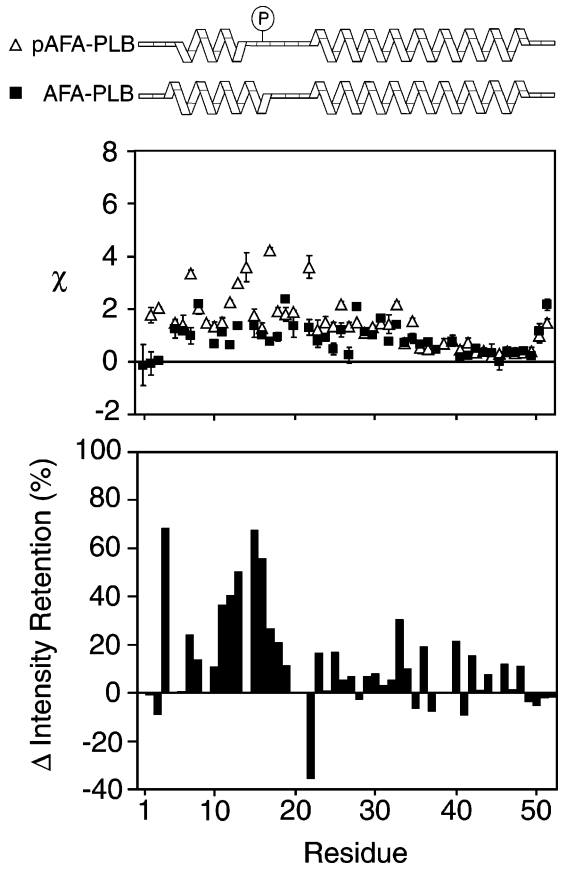

FIGURE 9: (Top) Comparison of the exchange factors (χ) for both AFA-PLB and pAFA-PLB. (Bottom) Histogram showing the difference in intensity retention in pAFA-PLB and AFA-PLB upon addition of Mn^{2+} ions. Positive values indicate that phosphorylation caused the residues to be more exposed to the bulk solvent; negative values show that phosphorylation caused the residue to be less exposed to the bulk solvent.

that domain Ib is more mobile and could be responsible for molding PLB into SERCA and other binding partners such as protein kinase A and phosphatase 1.

The melting of the structured loop and the partial unwinding of the cytoplasmic helix also causes the amide resonances of these regions to be more exposed to paramagnetic quenching by Mn^{2+} ions. This is clearly shown in Figure 9, where a difference in the retention of the signal intensity in the HSQC experiments in the presence of Mn^{2+} ions is reported for both phosphorylated and unphosphorylated PLB as a function of the residue number. A positive value in Figure 9 means that phosphorylation of AFA-PLB increases exposure of that resonance to the bulk solvent. While the pattern for the transmembrane domain is identical in both species (i.e., the values in Figure 9 are close to 0), there is a substantial difference in the paramagnetic effects between phosphorylated versus unphosphorylated PLB for residues 11−18. In addition, residue 4 seems to be more prone to paramagnetic quenching, while residue 22 shows opposite behavior. One possibility is that the conformational and dynamic changes caused by phosphorylation affect these residues by exposing (residue 4) or protecting (residue 22) them from the Mn^{2+} ions.

Nonetheless, on the basis of these results it is not possible to give the exact topology of the cytoplasmic domains of pAFA-PLB. Solid-state NMR experiments are underway to

determine whether the residual cytoplasmic helix lies parallel to the lipid bilayer or undergoes free motion in the bulk solvent.

Functional Implications. Previous high-resolution studies of the effect of S16 phosphorylation on PLB have been limited to synthetic fragments derived from the PLB primary sequence and dissolved in organic solvents. Our investigation is the first to show the effects of the phosphoryl transfer on S16 of the full-length PLB monomer in a membrane-mimetic environment.

For our studies, we focused on a monomeric mutant of PLB (AFA-PLB), which has been shown to preserve full inhibitory function while being more amenable to spectroscopic studies (*11*−*16*). The biological significance of studying the monomeric form of PLB stems from the fact that inhibitory function is activated by the depolymerization of PLB into monomers and that the homopentamer is an inactive reservoir (*6*−*8*). Moreover, under our experimental conditions, SERCA, PLB, and PKA are all fully functional, giving our research biological significance.

Our structural findings on pAFA-PLB are in agreement with several other spectroscopic analyses carried out in micelles and organic solvents on small peptide fragments of PLB (*40*−*42*). In particular, our results support a previous investigation carried out on monomeric and pentameric PLB reconstituted in both lipids and micelles (*43*). From fluorescence quenching measurements and SDS−PAGE gel-shift analysis, these researchers concluded that in various membrane-mimetic environments, including detergents (sodium dodecyl sulfate, octyl glucoside) and lipids (DOPC), phosphorylation does not change the oligomerization state of PLB; rather it induces a localized structural change within the PLB protomer. Our data complement and enrich these studies, revealing the atomic details of both the conformational transition and the enhanced dynamics induced by phosphoryl group transfer. From the NMR structure of a phosphorylated fragment of PLB solubilized either in a trifluoroethanol/water mixture or in SDS micelles, Johnson and co-workers (*40*) concluded that a possible trigger mechanism for the conformational switch is the formation of a salt bridge between the protonated guanidinium side chain of R13 and the phosphoryl group of S16. On the other hand, Pollesello et al. (*42*), using NMR and structure minimization procedures in the presence of Coulombian interactions, found that a S16/T17 double-phosphorylated 1−36 N-terminal fragment of PLB in TFE/water mixture shows that R14 rather than R13 is proximal to S16. Although our average minimized structure supports a proposed salt bridge mechanism between R13 and S16 (Figure 5C), we conclude that since S16 is highly dynamic, with a heteronuclear NOE value less than 0.6, the formation of a stable salt bridge is unlikely.

While our data do not completely rule out the possibility of a transient salt bridge, they suggest that changes in net charge alone may not be able to account for the effects of phosphorylation and that the conformational switch may also be triggered by steric interactions between the phosphate group on S16 and spatially proximal residues.

Both conformational changes and dynamics may explain the changes in the protein−protein interactions observed in the transmembrane and cytoplasmic domains of SERCA and PLB. To this extent, our NMR investigation shows that phosphorylation at S16 not only induces local conformational changes (i.e., the loss of β-turn conformation for the short loop, residues 17−21, and the unwinding part of the cytoplasmic helix, residues 13−16) but also affects the entire protein backbone dynamics.

Recent NMR and EPR (*15*, *37*) studies show that free PLB exists in a conformational preequilibrium between two structural states. The existence of these structural states is encoded in the exchange terms of the micro- to millisecond dynamics NMR experiments and is even more apparent in the EPR experiments. Addition of SERCA induces a shift toward the more dynamically disordered of the two states, perturbing the preexisting structural equilibrium of PLB (*7*). The results presented in this paper support the presence of a structural preequilibrium and underscore the hypothesis that phosphorylation perturbs the conformational switch (see increased presence of the micro- to millisecond dynamics), causing considerable rearrangement of the PLB binding surface (*38*).

Recent data acquired for neonatal cardiac myocytes by Dillmann and co-workers (*44*) confirm the conformational changes in the PLB cytoplasmic domain, and using both in vitro and in vivo studies, they demonstrate that by mimicking PLB phosphorylation it is possible to devise new therapeutical strategies to increase cardiac contractility.

While our results shed new light on the conformational and dynamical transitions of PLB in the unbound state, further investigation of PLB bound to SERCA will be necessary. A recent fluorescence study limited to specific labeled sites of PLB suggests that this protein when bound to SERCA maintains a compact conformation, while upon the addition of PKA PLB is phosphorylated and its binding surface may be significantly different (*45*, *46*). The observed changes in local conformation as well as local and global dynamics that we observe sustain this interpretation. However, a better understanding of how phosphoryl transfer affects PLB interactions with SERCA will only become possible when the bound forms of PLB, both unphosphorylated and phosphorylated, are elucidated at the atomic level.

CONCLUSIONS

We report the NMR solution structure and ^{15}N backbone dynamics of AFA-PLB phosphorylated at S16 by cAMP-dependent protein kinase in DPC micelles. Upon phosphorylation, AFA-PLB loses its secondary structure around the phosphorylation site, resulting in an unstructured loop region between two α-helical domains with a concomitant loss of structural connections between the transmembrane and the cytoplasmic domains. Phosphorylation also increases the mobility of backbone motion across the entire protein, inducing opposite effects on R_1 and R_2 spin relaxation rates. These changes in dynamics reveal that while structural changes induced by phosphorylation are localized in the residues surrounding the phosphorylation site, the changes in dynamics extend throughout the entire protein. These results are significant for understanding how the addition of a phosphate group at S16 disrupts the interactions of residues with SERCA in both the cytoplasmic and transmembrane domains of the protein.

ACKNOWLEDGMENT

We thank Professor D. Thomas for many helpful discussions and for critical reading of our manuscript. We thank Dr. Jamillah Zamoon and Bethany Buck for helpful discussions, Beverly Ostrowski and David Live at the Nuclear Magnetic Resonance Facility at the University of Minnesota for assistance with NMR experiments, and Tom Crick at the Mass Spectrometry Consortium for the Life Sciences at the University of Minnesota for assistance with the analysis of phosphorylated PLB. Also, we thank Professor E. Zuiderweg for providing the pulse program for the analysis of the slow NMR dynamics and helpful discussion. Finally, we thank Debbie Pierson and Kim Ha for assistance with the preparation and phosphorylation of AFA-PLB.

REFERENCES

1. Chu, G., and Kranias, E. G. (2002) Functional interplay between dual site phospholambam phosphorylation: insights from genetically altered mouse models, *Basic Res. Cardiol. 97*, 143−148.
2. Hoshijima, M., Ikeda, Y., Iwanaga, Y., Minamisawa, S., Date, M. O., Gu, Y., Iwatate, M., Li, M., Wang, L., Wilson, J. M., Wang, Y., Ross, J. J., and Chien, K. R. (2002) Chronic suppression of heart-failure progression by a pseudophosphorylated mutant of phospholamban via in vivo cardiac rAAV gene delivery, *Nat. Med. 8*, 984−871.
3. Iwanaga, Y., Hoshijima, M., Gu, Y., Iwatate, M., Dieterle, T., Ikeda, Y., Date, M. O., Chrast, J., Matsuzaki, M., Peterson, K. L., Chien, K. R., and Ross, J. J. (2004) Chronic phospholamban inhibition prevents progressive cardiac dysfunction and pathological remodeling after infarction in rats, *J. Clin. Invest. 113*, 727−736.
4. Schmitt, J. P., Kamisago, M., Asahi, M., Li, G. H., Ahmad, F., Mende, U., Kranias, E. G., MacLennan, D. H., Seidman, J. G., and Seidman, C. E. (2003) Dilated cardiomyopathy and heart failure caused by a mutation in phospholamban, *Science 299*, 1410−3.
5. James, P., Inui, M., Tada, M., Chiesi, M., and Carafoli, E. (1989) Nature and site of phospholamban regulation of the Ca^{2+} pump of sarcoplasmic reticulum, *Nature 342*, 90−2.
6. Kimura, Y., Kurzydlowski, K., Tada, M., and MacLennan, D. H. (1997) Phospholamban inhibitory function is activated by depolymerization, *J. Biol. Chem. 272*, 15061−4.
7. Zamoon, J., Nitu, F., Karim, C. B., Thomas, D. D., and Veglia, G. (2004) Mapping the Binding Epitope of an Integral Membrane Protein: Unveiling the Conformational Switch in Phospholamban Regulation of SERCA, *Proc. Natl. Acad. Sci. U.S.A.* (in press).
8. Arkin, I. T., Adams, P. D., Brunger, A. T., Smith, S. O., and Engelman, D. M. (1997) Structural perspectives of phospholamban, a helical transmembrane pentamer, *Annu. Rev. Biophys. Biomol. Struct. 26*, 157−179.
9. Cornea, R. L., Jones, L. R., Autry, J. M., and Thomas, D. D. (1997) Mutation and phosphorylation change the oligomeric structure of phospholamban in lipid bilayers, *Biochemistry 36*, 2960−2967.
10. Fujii, J., Maruyamma, K., Tada, M., and MacLennan, D. H. (1989) Expression and site-specific mutagenesis of phospholamban. Studies of residues involved in phosphorylation and pentamer formation, *J. Biol. Chem. 264*, 12950−12955.
11. Karim, C. B., Marquardt, C. G., Stamm, J. D., Barany, G., and Thomas, D. D. (2000) Synthetic null-cysteine phospholamban analogue and the corresponding transmembrane domain inhibit the Ca-ATPase, *Biochemistry 39*, 10892−7.
12. Karim, C. B., Stamm, J. D., Karim, J., Jones, L. R., and Thomas, D. D. (1998) Cysteine reactivity and oligomeric structures of phospholamban and its mutants, *Biochemistry 37*, 12074−81.
13. Zamoon, J., Mascioni, A., Thomas, D. D., and Veglia, G. (2003) NMR solution structure and topological orientation of monomeric phospholamban in dodecylphosphocholine micelles, *Biophys. J. 85*, 2589−98.
14. Mascioni, A., Karim, C., Zamoon, J., Thomas, D. D., and Veglia, G. (2002) Solid-state NMR and rigid body molecular dynamics to determine domain orientations of monomeric phospholamban, *J. Am. Chem. Soc. 124*, 9392−3.
15. Metcalfe, E. E., Zamoon, J., Thomas, D. D., and Veglia, G. (2004) $^{1}H/^{15}N$ Heteronuclear NMR Spectroscopy Shows Four Dynamic Domains for Phospholamban Reconstituted in Dodecylphosphocholine Micelles, *Biophys. J. 87*, 1−10.
16. Buck, B. Zamoon, J., Kirby, T. L., De Silva, T. M., Karim, C. B., Thomas, D. D., and Veglia, G. (2003) Overexpression, purification and characterization of recombinant Ca-ATPase regulators for high-resolution and solid-state NMR spectroscopy, *Protein Expression Purif. 30*, 253−261.
17. Parks, T. D., Leuther, K. K., Howard, E. D., Johnson, S. A., and Dougherty, W. G. (1994) Release of peptides and proteins from fusion proteins using a recombinant plant virus proteinase, *Anal. Biochem. 216*, 413−417.
18. Mayer, E. J., Huckle, W., Johnson, R. G. J., and McKenna, E. (2000) Characterization and quantitation of phospholamban and its phosphorylation state using antibodies, *Biochem. Biophys. Res. Commun. 267*, 40−48.
19. Marion, D., Ikura, M., Tschudin, R., and Bax, A. (1989) Rapid recording of 2D NMR spectra without phase cycling. Application to the study of hydrogen exchange in proteins, *J. Magn. Reson. 85*, 393−399.
20. Shaka, A. J., Barker, P. B., and Freeman, R. (1985) Computer-optimized decoupling scheme for wideband applications and low-level operation, *J. Magn. Reson. 64*, 547−552.
21. Marion, D., Kay, L. E., Sparks, S. W., Torchia, D. A., and Bax, A. (1989) Three-Dimensional Heteronuclear NMR of ^{15}N-Labeled Proteins, *J. Am. Chem. Soc. 11*, 1515−1517.
22. Wishart, D. S., Bigam, C. G., Holm, A., Hodges, R. S., and Sykes, B. D. (1995) ^{1}H, ^{13}C and ^{15}N random coil NMR chemical shifts of the common amino acids. I. Investigations of nearest-neighbor effects, *J. Biomol. NMR 5*, 67−81.
23. Wishart, D. S., Bigam, C. G., Yao, J., Abildgaard, F., Dyson, H. J., Oldfield, E., Markley, J. L., and Sykes, B. D. (1995) ^{1}H, ^{13}C and ^{15}N chemical shift referencing in biomolecular NMR, *J. Biomol. NMR 6*, 135−40.
24. Delaglio, F., Grzesiek, S., Vuister, G. W., Zhu, G., Pfeifer, J., and Bax, A. (1995) NMRPipe: a multidimensional spectral processing system based on UNIX pipes, *J. Biomol. NMR 6*, 277−93.
25. Johnson, B. A., and Blevins, R. A. (1994) A computer program for the visualization and analysis of NMR data, *J. Biomol. NMR 4*, 603−614.
26. Schwieter, C. D., Kuszewski, J. J., Tjandra, N., and Clore, G. M. (2003) The X-PLOR-NIH NMR molecular structure determination package, *J. Magon. Reson. 160*, 66−74.
27. Laskowski, R. A., MacArthur, M. W., and Thornton, J. M. (1998) Validation of protein models derived from experiment, *Curr. Opin. Struct. Biol. 8*, 631−9.
28. Farrow, N. A., Muhandiram, R., Singer, A. U., Pascal, S. M., Kay, C. M., Gish, G., Shoelson, S. E., Pawson, T., Forman-Kay, J. D., and Kay, L. E. (1994) Backbone dynamics of a free and phosphopeptide-complexed Src homology 2 domain studied by ^{15}N NMR relaxation, *Biochemistry 33*, 5984−6003.
29. Palmer, A. G., III, Skelton, N. J., Chazin, W. J., Wright, P. E., and Rance, M. (1992) Suppression of the effects of cross-relaxation between dipolar and anisotropic chemical shift relaxation mechanisms in the measurements of spin−spin relaxation rates, *Mol. Phys. 75*, 699−711.
30. Skelton, N. J., Palmer, A. G., III, Akke, M., Kördel, J., Rance, M., and Chazin, W. (1993) Practical aspects of two-dimensional proton detected ^{15}N spin relaxation measurements, *J. Magn. Reson., Ser. B 102*, 253−264.
31. Palmer, A. G., III, Rance, M., and Wright, P. E. (1991) Intramolecular motions of a zinc finger DNA-binding domain from Xfin characterized by proton-detected natural abundance ^{13}C heteronuclear NMR spectroscopy, *J. Am. Chem. Soc. 113*, 4371−4380.
32. Mandel, A. M., Akke, M., and Palmer, A. G. (1995) Backbone dynamics of *Escherichia coli* ribonuclease H1: Correlations with structure and function in an active enzyme, *J. Mol. Biol. 246*, 144−163.
33. Wang, L., Pang, Y., Holder, T., Brender, J. R., Kurochkin, A. V., and Zuiderweg, E. R. (2001) Functional dynamics in the active site of the ribonuclease binase, *Proc. Natl. Acad. Sci. U.S.A. 98*, 7684−7689.
34. Veglia, G., Zeri, A. C., Ma, C., and Opella, S. J. (2002) Deuterium/hydrogen exchange factors measured by solution nuclear magnetic resonance spectroscopy as indicators of the structure and topology of membrane proteins, *Biophys. J. 82*, 2176−83.

35. Damberg, P., Jarvet, J., and Graslund, A. (2001) Micellar systems as solvents in peptide and protein structure determination, *Methods Enzymol. 339*, 271−85.
36. Wuthrich, K. (1986) *NMR of Proteins and Nucleic Acids*, John Wiley and Sons, Inc., New York.
37. Karim, C. B., Kirby, T. L., Zhang, Z., Nesmelov, Y., and Thomas, D. D. (2004) Phospholamban structural dynamics in lipid bilayers probed by a spin label rigidly coupled to the peptide backbone, *Proc. Natl. Acad. Sci. U.S.A. 101*, 14437−14442.
38. Chen, B., and Bigelow, D. J. (2002) Phosphorylation induces a conformational transition near the lipid−water interface of phospholamban reconstituted with the Ca-ATPase, *Biochemistry 41*, 13965−13972.
39. Lipari, G., and Szabo, A. (1982) Model-Free Approach to the interpretation of nucler magnetic resonance relaxation of macromolecules, *J. Am. Chem. Soc. 104*, 4559−4570.
40. Mortishire-Smith, R. J., Pitzenberger, S. M., Burke, C. J., Middaugh, C. R., Garsky, V. M., and Johnson, R. G. (1995) Solution structure of the cytoplasmic domain of phospholamban: phosphorylation leads to a local perturbation in secondary structure, *Biochemistry 34*, 7603−7613.
41. Pollesello, P., Annila, A., and Ovaska, M. (1999) Structure of the 1−36 amino-terminal fragment of human phospholamban by nuclear magnetic resonance and modeling of the phospholamban pentamer, *Biophys. J. 76*, 1784−95.
42. Terzi, E., Poteur, L., and Trifilieff, E. (1992) Evidence for a phosphorylation-induced conformational change in phospholamban cytoplasmic domain by CD analysis, *FEBS Lett. 309*, 413−416.
43. Cornea, R. L., Autry, J. M., Jones, L. R., and Thomas, D. D. (1998) Phosphorylation-induced structural change in phospholamban and its mutants, detected by intrinsic fluorescence, *Biochemistry 37*, 7869−7877.
44. Meyer, M., Belke, D. D., Trost, S. U., Swanson, E., Dieterle, T., Scott, B., Cary, S. P., Ho, P., Bluhm, W. F., McDonough, P. M., Silverman, G. J., and Dillman, W. H. (2004) A recombinant antibody increases cardiac contractility by mimicking phospholamban phosphorylation, *FASEB J. 18*, 1312−1314.
45. Li, J., Bigelow, D. J., and Squier, T. C. (2003) Phosphorylation by cAMP-dependent protein kinase modulates the structural coupling between the transmembrane and cytosolic domains of phospholamban, *Biochemistry 42*, 10674−10682.
46. Squier, T. C., and Bigelow, D. J. (2004) Conformational changes within the cytosolic portion of phospholamban upon release of Ca-ATPase inhibition, *Biochemistry 43*, 3870−3879.

BI047571E